

Analysis and Qualitative Effects of Large Breasts on Aerodynamic Performance and Wake of a “Miss Kobayashi’s Dragon Maid” Character

N. Rabino

ARTICLE INFO

Keywords:

Computational fluid dynamics, ANSYS, drag coefficient, human aerodynamics, SST k- ω model, anime, Quetzalcoatl, titties, thicc

AMS Subject Classifications:

00A72, 76-05, 76G25

ABSTRACT

A computational fluid dynamics methodology is used to study the salient flow features around the breasts of a human figure and to describe the aerodynamic differences imparted by their geometric presence. Two models are proposed for examination: a 3-dimensional reference based on a character design with a significantly buxom figure and a modification of this design where the breast size is reduced significantly. The two models are tested at speeds ranging from 1 to 30 m·s⁻¹ using Reynolds-averaged Navier Stokes (RANS). Drag, lift, and skin friction forces, along with turbulence kinetic energy (TKE), are investigated and compared between the different models. The present results are expected to provide useful information on the validity of the statement, “Flat is Justice” in terms of an aerodynamic standpoint. In addition to this, the results can offer worthwhile data investigating the anthropometrical presence of large breasts on sport aerodynamics.

1. Introduction

The aerodynamics of the human form has been an area of valuable research in various aspects of sports and competition. Air resistance (hereinafter referred to as “drag”) is a concerning factor in many time-based trials, and enhancing potential efficiency can be done through the elucidation of the flow around the human figure. Studies concerning the drag of the human body using wind tunnels can be found dating back to the 1920s [1]. A small sampling of subsequent studies exploring the effect of drag covers areas such as running [2], cycling [3], skiing [4], and skating [5], all of which reinforces the relevance of aerodynamic investigation on the human shape in regards to performance.

In many of such studies, the authors seek to investigate the effect of positioning in relation to drag [6], and some utilize numerous subjects of differing anthropometric proportions to describe a generalized result on such positioning [7, 8]. Hitherto, none within the author’s investigations has described the effect of specific physiological features on aerodynamic performance in great detail. Stemming from certain internet communities and pertinent to the current era comes the succinct statement, “Flat is Justice”, which consequentially begets interesting debate that can reverberate and diffuse throughout media. Essentially, the statement describes the appreciation of flat-chested women [9], which posits a peculiar aspect that has yet to be fully explored in human aerodynamics; namely, the effect of breasts in regards to drag and overall aerodynamic performance.

This work is intended to contribute to the understanding of how large breasts can affect the dynamics of the human wake through the use of computational fluid dynamics (CFD) simulation tools. This preliminary work focuses solely on comparing the relevant effects of large breasts of a selected human design to that of the same design but with, euphemistically, “lesser tracts of land”. The following sections will present an overall understanding on the human wake in relation to simplified geometry along with engineering applications, introduce the chosen human geometry and models, relevant boundary conditions, the governing equations, and the numerical methods used to solve the equations. An in-depth review on the computational uncertainty is described, following with extensive results and discussion, conclusions, and recommendations for future work.

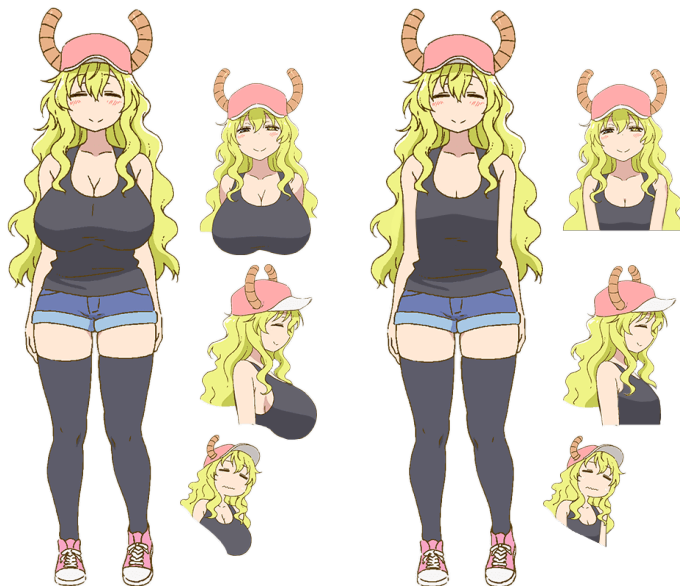
1.1 Background on the Human Wake

The human body can best be described as a bluff-body in respect to the flow around it. Literature on the behavior of the wakes behind bluff bodies indicates that the flow will be unsteady due to the turbulent transition and separation of the boundary layer [10]. A simplification analo-

gous to the human shape can be represented by a grouping of uniform circular cylinders [11] and therefore existing studies on this type of geometry can provide general insight into the wake region. Sumner et al. [12] described the wake and development of vortex structures of cylinders with aspect ratios (i.e. height to diameter) of 3, 5, and 9, and determined that a transition in vortex shedding occurs at $h/d = 3$. An investigation by Okamoto and Sunabashiri [13] also supports this finding, adding that cylinders with an aspect ratio of 3 experience a recirculation region that extends four diameters downstream. Assuming the human form takes on a roughly large cylindrical shape near this aspect ratio, it is to be expected that the recirculation region will behave similarly and extend approximately four body widths downstream.

A readily apparent deviation in geometry compared to studies done on singular cylinders is the presence of the gap between the legs. An extensive and comprehensive review done by Zhou and Alam [14] on the various arrangements of two cylinders indicate the wake structure falls into a multitude of regimes. In a side-by-side configuration, being similar to the two legs of a human, it is deduced that there are three primary regimes where the wake experiences proximity interference. When closely spaced together, the first regime shows that the cylinders act similarly to that of a single bluff body with a width corresponding to the two cylinders. When the gap width is larger than 20% of the diameter, each cylinder has individual wakes that strongly affect one another and is associated with the second regime. At gap widths exceeding approximately 100–120% of the diameter, each cylinder acts as an independent body with the vortex streets being loosely influenced by one another. Seeing that human legs are not strictly cylinders with a fixed diameter but more akin to inverted tapered cylinders, the wakes behind the legs will likely behave in a similar fashion observed in both the first and second regime. With the ankles and calves being narrower and having a larger gap between them, the second regime is applicable. A transition into the first regime can be expected associated with the bulkiness of the thighs and reduction in gap width.

Engineering literature can also provide additional details on the flow characteristics around the body. Many of such studies are motivated by exposure control and contaminant transport [15, 16], thermal issues [17, 18], and comfort prediction [19], rather than overall drag effects. Inherently, many of the tested flow characteristics are evaluated in a quiescent environment or at air velocities that are of a lower order compared to those found in sport-related studies. Nonetheless, these studies provide useful insight on the natural turbulence caused by the human form and the expected anatomical location of flow separation. Inthavong et al. [20] utilized a high speed camera to record the wake generation of a 1/5th scaled realistic human manikin that was accelerated to a velocity of ~ 1 m·s⁻¹. From their results, it was found that the



(a) Original reference design. Courtesy: Kyoto Animation. (b) The modified design proposed for comparison.

Figure 1. Comparison of different designs for Lucoa.



Figure 2. A perspective measurement of Lucoa in reference to a door frame using the Vanishing Point Tool in Adobe Photoshop.

shoulder undergoes flow separation and produces vortices in a regular pattern. The hands produce a well-defined yet unstable vortex sheet that curls towards the centerline of the body. The head acts similarly to classical sphere/cylinder cases with the addition of a trailing wake forming from behind the neck. The neck was found to remove the expected counter free shear layer that is present in cylinder studies and thus eliminates the formation of an oscillating vortex sheet. In all, it can be said that the observed human wake is a highly complex and richly diverse system that is easily influenced by the inherent geometry used; it is expected that from this study, an overall summary can be presented on how and to what degree the previously described flow structures are affected by the presence of large breasts.

2. Methodology

2.1 Design Proposal and Model Scaling

The use of realistic human models affords greater realization of the pertinent flow characteristics as they are considerably different than those of generalized models. Yan et al. [21] concluded that an excessive degree of simplification in using a manikin can affect the ability to achieve accurate results, and thus precludes the use of a simplified model for this study. However, the acquisition of a 3-D scanned human model with a significant bust undoubtedly proved difficult. The use of a highly unconventional approach was used to ameliorate this issue.

The animated adaptation of *Miss Kobayashi's Dragon Maid*, being a recently popular show [22] and spawning a sizable subculture on the internet [23], proved suitable in terms of providing potential models. The dragon characters (themselves being based off of mythically and culturally prominent dragons) assume a human form to interact with other humans in this well-received [24] slice-of-life urban fantasy. A majority of the human forms of the female dragon characters possessed significant busts. However, Quetzalcoatl (referred to canonically as "Lucoa" and will be named as such throughout the rest of this paper) substantiated herself as the adaptation's gag character by her significant size [25, 26], thus making her the perfect candidate in providing a suitable model. Being clearly the largest amongst her fellow dragons as established in Figure 1, Lucoa provides the best contrast between a large bust and having none at all. To provide the most direct comparison in regards to the effect of large breasts on the wake, a dramatic reduction in bust size as reflected in Figure 1(b) was proposed for use in this study.

In order to obtain accurate results from the setups described later in this paper, it is important to have the subject in question reflect real world scales properly. Lucoa's height while in human form is not given explicitly in any related media within the scope of the author's research. Thus, Lucoa's height must be estimated in relation to objects of which a reasonable measurement can readily be found. Conveniently, there is a scene found within Episode 6, Season 1 of the animated adaptation wherein Lucoa steps through a doorway. Assuming the door is of a typical size¹ used for external entrances, in addition to Lucoa being scaled properly in the scene, we can estimate her height using a vanishing point technique.

Using the door as depicted in Figure 2 to judge Lucoa's height, it was determined that she stands approximately 177 cm measured to the top of her hat, with her horns boosting her overall figure to a height of 182 cm. These numbers can be considered reasonable based on canonical descriptions of Lucoa's towering stature [27] compared to the average height of 158 cm for a Japanese woman [28].

2.2 3-Dimensional Models and Geometry Analysis

Since Lucoa is a fictional character that is commonly portrayed in a 2-dimensional² world, determining her form drag between the two proposed designs as described in Figure 1 requires that we add another dimension to her model. Conveniently enough, an available 3-D model of Lucoa [29] was used that would make the simulation possible. This *MikuMikuDance* 3-D model (henceforth referred to as the "Normal" model) was then imported into the 3-D modeling program Blender, scaled to the determined height as described in the previous section, then exported into an STL file. This STL file was then repaired using the built-in repair feature present in Microsoft 3D Builder due to the unclear geometry inherent with the model. To achieve the modified design (henceforth referred to as the "Flat" model), the original *MikuMikuDance* model was modified using the built-in tools in Blender to dramatically reduce Lucoa's breast size. The export and repair process remained the same as for the original model.

As shown in Figure 3, all positions between the two models remain the same and left unperturbed to leave the reduction in breast size as the sole geometric difference to be investigated. Although the typical orthostatic (standing) orientation of a human has the upper limbs in a

¹ A typical metric external door's size is 926 mm wide by 2040 mm tall.

² Referring to the media she is portrayed in, such as printed materials and television.

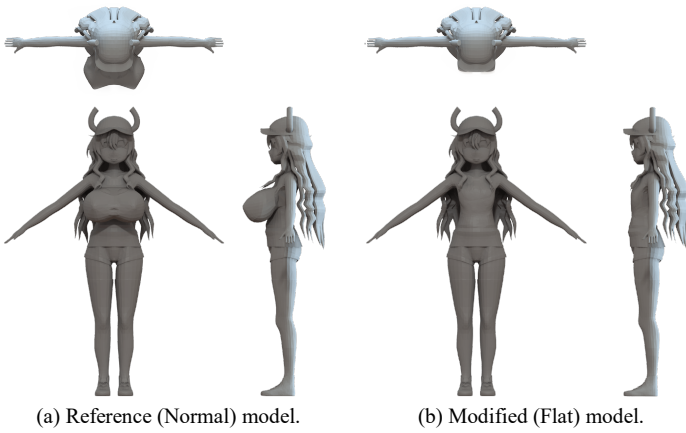


Figure 3. 3-D representations of Lucoa to be used in CFD simulations, detailing (clockwise) top, side, and front views.

relaxed position [30], the arms are left posed at a 45° adduction angle from the torso, as this is the default ‘A’ pose when importing the model. This arm position also has an advantage in this study as it potentially enables a more thorough analysis on the effect of breasts on the wake region, whereas a neutral standing posture would have the arms interfere with the downstream effect of the breasts. The hair is left modeled as solid to reduce simulation complexity and setup.³ While humans naturally lean forward against the direction of the wind to maintain equilibrium [31], this factor is not considered in this study as this leaning would change the frontal area exposed to the fluid flow and thus complicate comparisons against static reference models.

Dimensionally, the bounds of the two models are similar, with the height and arm span being 1.82 and 1.387 meters respectively. The Normal model has a depth of 0.525 meters whereas the Flat model is only 0.414 meters. The frontal projected area, A , of both models is 0.584 m². The volumetric difference between the two is 9.19 L, indicating that each breast on the Normal model has an enormous volume of approximately 4.6 L. The under-bust circumference of the Normal model is approximately 64 cm and the bust measures 115 cm. The Flat model has the same under-bust measurement whereas the bust measures 68 cm. Attempting to match the dimensions and bust volume of the Normal model to existing cup sizing scales is difficult as these measurements are exceptionally large and exceed volumes measured in other studies [32]. Using the JIS L 4006:1998 [33] scale and extrapolating⁴ cup sizing from the largest listed size (I-cup), the Normal model can be described as being 10 cups larger; an estimated “S65”. The Flat model is a stark contrast to this, where it matches a petite “AA65” size.

The dramatic difference in bust size between the models serves to provide the most significant change in outcomes; it is assumed that due to the absurd bust size, any size smaller than the Normal model would have an outcome that would fall in a range between both models.

2.3 Evaluated Metrics and Implementation

Four metrics under investigation for this study include drag and lift forces (including their associated coefficients), skin friction coefficient, and finally, turbulence kinetic energy. To evaluate the drag coefficient, C_D , and drag force, F_D , the following equations are used,

$$C_D = \frac{2F_D}{\rho U_\infty^2 A} \quad (1)$$

$$F_D = \int_A (-P \cos \theta + \tau_w \sin \theta) dA \quad (2)$$

³ Hair physics is beyond the scope of the author, and thus this study, due to the inordinate amount of computing resources and time needed to setup and simulate hair strands in a physically accurate fashion.

⁴ In [33], each cup size is binned with every 2.5 cm deviation from the under-bust measurement starting from 7.5 cm.

where ρ is the fluid density, U_∞ is the free stream velocity, A is the frontal projected area, and P is the pressure at the surface dA . τ_w is the local wall shear stress being defined as,

$$\tau_w \equiv \mu \left. \frac{\partial u}{\partial y} \right|_{y=0} \quad (3)$$

with μ as the dynamic viscosity, u the flow velocity along the boundary, and y being the height above the boundary. The value of C_D is not constant and is dependent on Reynolds number, which is defined as,

$$Re = \frac{\rho u L}{\mu} \quad (4)$$

where L is an arbitrary characteristic length. In this study, L is equal to the height of the models.

The lift coefficient is comparable to the drag coefficient, being that the force is evaluated in a direction that is perpendicular to the mean flow direction, e.g. vertically upwards. Thus,

$$C_L = \frac{2F_L}{\rho U_\infty^2 S} \quad (5)$$

$$F_L = \int_A (-P \sin \theta + \tau_w \cos \theta) dA \quad (6)$$

Instead of the frontal projected area, A , a reference surface area, S , is used. For consistent comparison however, A and S are left defined as being equivalent, thus $A = S$. This result does not affect the calculated forces but rather only the coefficient, and as such, the lift coefficient is dependent on the frontal area.

The skin friction coefficient, C_f , is evaluated in a similar manner to the drag coefficient since the force attributed to skin friction is a component of the profile drag, F_D . Therefore,

$$C_f = \frac{2\tau_w}{\rho U_\infty^2} \quad (7)$$

Analyzing the skin friction coefficient allows insight into areas where the boundary layer thickness changes; as turbulent flow increases, the thickness of the boundary layer increases, and consequently areas where C_f transitions to larger values or experiences spikes are indicative of where flow separation is prevalent [34, 35].

Turbulence kinetic energy (TKE) signifies the loss of kinetic energy from the mean flow and represents the energy present with eddies in turbulent flow; it is a direct measure of the intensity of turbulence. In a general form quantifying the mean of turbulence normal stresses, TKE is defined as,

$$k = \frac{1}{2} (\overline{(u')^2} + \overline{(v')^2} + \overline{(w')^2}) \quad (8)$$

The exact value of TKE is calculated based on the closure of the Reynolds-averaged Navier-Stokes equations, which is further discussed in Section 3.3.

The numerical simulations in this present work, along with the automatic evaluation of the equations described in this section, were carried out using ANSYS FLUENT R17. The 3-D models defined in Section 2.2 were imported into FLUENT and followed the methodology as described in the following section.

3. Computational Fluid Dynamics (CFD) Setup and Analysis

3.1 Boundary Conditions

The use of boundary conditions based on real-world environments enhances the overall applicability of the results stemming from the simulations. It was therefore important to determine the most appropriate and accurate environment in which to simulate the models with. It was

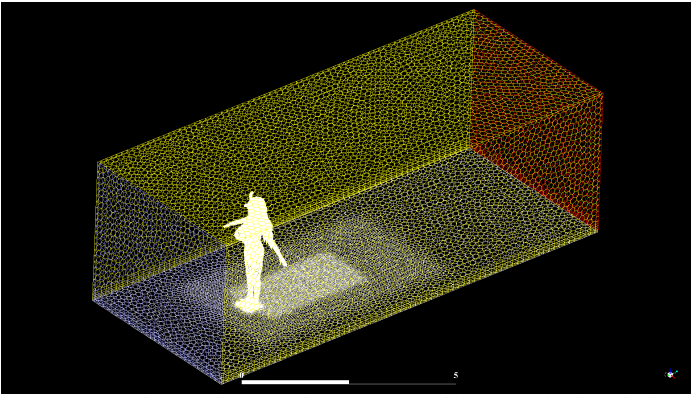


Figure 4. Boundary conditions of the computational domain, with the inlet being represented in blue, outlet in red, walls in white, and symmetry in yellow.

found that the overall location used in the animated adaptation of *Miss Kobayashi's Dragon Maid* was based on the city of Koshigaya [36], situated in the Saitama Prefecture of Japan. A logical time of year to assume a person being outside without excess clothing would be sometime in the summer. Using the month of August, it was found that weather conditions in Koshigaya and nearby surrounding regions feature averages [37] of 22.6°C for temperature, 73% for relative humidity, and 1005.9 hPa for local atmospheric pressure. Thus, the air density was calculated to be $\rho = 1.1581 \text{ kg} \cdot \text{m}^{-3}$ and the dynamic viscosity to be $\mu = 1.86847 \cdot 10^{-5} \text{ kg} \cdot \text{m}^{-1} \cdot \text{s}^{-1}$.

Since the human body can vary based upon the clothing worn, surface roughness and the effects of fabrics are parameters that are ignored in this study. Although multiple studies have shown fabrics have a noticeable effect on the overall drag of a human body [7, 38], the walls in this computational work can be regarded as smooth. In all simulations, the models and ground of the domain are modeled as non-moving walls with no-slip conditions. The clothing that is part of the models is treated in the same manner.

Table 1. Summary of boundary conditions in the present study.

Wind speed	U_∞	$\text{m} \cdot \text{s}^{-1}$	1.0, 2.5, 5.0, 7.5, 10.0, 15.0, 20.0, 25.0, 30.0
Reynolds Number	Re	—	$1.281 \cdot 10^5 \sim 3.384 \cdot 10^6$
Domain bounds	—	m	$\begin{cases} -1.44 \leq x \leq 1.44 \\ -2.34 \leq y \leq 5.65 \\ 0 \leq z \leq 2.32 \end{cases}$
Turbulent intensity	I_{inlet}	—	1%
	$I_{\text{outlet,backflow}}$	—	5%
Turbulent viscosity ratio	$\left(\frac{\mu_t}{\mu}\right)_{\text{inlet}}$	—	10
	$\left(\frac{\mu_t}{\mu}\right)_{\text{outlet,backflow}}$	—	10
Outlet gauge pressure	P_g	Pa	0

Inlet velocities range from $1 \text{ m} \cdot \text{s}^{-1}$ to $30 \text{ m} \cdot \text{s}^{-1}$ in the positive y -direction (since in this respect, the positive z -direction refers to the “up” orientation; refer to Figure 4 for clarification), highlighting typical wind speeds encountered on a day-to-day basis such as walking [39] all the way up to standing in a violent storm [40]. At the inlet, turbulence is specified using both turbulence intensity, I , and turbulent viscosity ratio, μ_t/μ . Turbulence intensity is defined as the ratio of the root-mean-square of velocity fluctuations, u' , to the mean flow velocity, U_∞ , and the turbulent viscosity ratio being directly proportional to the turbulent Reynolds number ($Re_t \equiv k^2/\epsilon\nu$). These values are summarized in Table 1.

The boundary condition at the outlet is treated as a pressure outlet where a static gauge pressure is specified. In this case, turbulence is specified similarly as the inlet but regarded in terms of “backflow”,

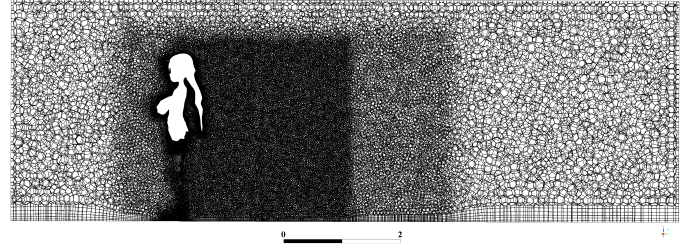


Figure 5. Side view of the full grid domain along the median plane.

should the flow reverse direction at the boundary during iterative calculations. The remaining borders of the “virtual wind tunnel” are modeled as symmetric to simulate zero-shear slip walls. In FLUENT, this boundary condition assumes a zero flux for all quantities, which imposes a zero normal gradient across the defined boundary and thus enforces a parallel flow.

In FLUENT, the flow is initialized with a velocity field equal to the specified velocity for the run, e.g., a run specified at $1.0 \text{ m} \cdot \text{s}^{-1}$ would have the entire field initialized with that value, and so on. Turbulence parameters at the boundaries are also initialized based on turbulence values as specified in Table 1. The blockage ratio was determined to be 8.7%, which would necessitate the usage of a correction factor to data; however, a blockage ratio of up to 10% in regards to bluff bodies has shown to provide reasonably similar outcomes compared to testing using lower blockage ratios [41] and therefore a correction factor was not used.

3.2 Grid Generation

The computational domain was discretized with an unstructured grid as shown in Figure 5. To reduce numerical diffusion and to more accurately resolve the viscous boundary layer, the surface grids on the models and ground were extruded using prismatic elements that are sized appropriately to the aspect ratio of their associated surface cell. These prisms are grown to 5 layers and follows recommendations put forth by Lanfrit [42]. Two prismatic bodies of influence (BOI) of increasing refinement are used to improve the resolution of the grid in both the wake region and the surrounding area around the models to sufficiently capture turbulence and flow separation. This is done to ensure that computational processing is focused on more important regions in the flow regime while keeping the far field sufficiently coarse enough as to not dramatically hamper computational time. The overall grid is limited to a maximum spacing of 0.1 m and a minimum of 2 mm. The smaller, finer BOI is sized by the bounds $-0.894 \leq x \leq 0.894$, $-0.1 \leq y \leq 2.76$, $0 \leq z \leq 1.87$ and the larger, coarser BOI defined by $-0.944 \leq x \leq 0.944$, $-1 \leq y \leq 4.26$, $0 \leq z \leq 1.92$, all in meters.

A conversion algorithm in FLUENT was used to convert the preliminary tetrahedral and prismatic grid into a polyhedral one. Polyhedra exhibit advantages over tetrahedra, namely, they approximate gradients better than tetrahedra due to the fact they are bounded by many neighbors. Additionally, polyhedra have more lax geometric criteria due to their insensitivity to stretching, making grid pre- and post-processing easier; this is well suited to the highly complex geometry of the models used. It has been observed that polyhedral grids provide the same level of accuracy as tetrahedral ones, but of significantly lower element count, thereby hastening simulations [43]. Furthermore, polyhedral grids have shown to improve convergence while having notably greater accuracy under unsteady simulations [44]. This is further supported by similar external aerodynamic studies run under FLUENT, where speedups between 2 to 3 times towards a converged solution have been observed [45].

3.3 Turbulence Model and Computational Approach

The flow around the models is modeled with Reynolds-averaged Navier-Stokes (RANS) equations in incompressible form. Written in Cartesian tensor form and having flow variables of the form $\phi = \bar{\phi} + \phi'$ (with $\bar{\phi}$ and ϕ' being the mean and fluctuating components respectively)

being substituted into the instantaneous continuity and momentum equations of the exact Navier-Stokes equations, we obtain [46]

$$\frac{\partial \rho}{\partial t} + \frac{\partial}{\partial x_i}(\rho u_i) = 0 \quad (9)$$

$$\begin{aligned} & \frac{\partial}{\partial t}(\rho u_i) + \frac{\partial}{\partial x_j}(\rho u_i u_j) \\ &= -\frac{\partial p}{\partial x_i} + \frac{\partial}{\partial x_j} \left[\mu \left(\frac{\partial u_i}{\partial x_j} + \frac{\partial u_j}{\partial x_i} - \frac{2}{3} \delta_{ij} \frac{\partial u_l}{\partial x_l} \right) \right] + \frac{\partial}{\partial x_j}(-\rho \overline{u_i' u_j'}) \end{aligned} \quad (10)$$

The closure of the set of equations are done by means of Menter’s two-equation blended $k-\varepsilon / k-\omega$ shear stress transport (SST) model [47] which computes eddy viscosity with a linear stress-strain closure. Menter’s model combines and smoothly blends the individual strengths of the $k-\varepsilon$ and $k-\omega$ models, where the $k-\varepsilon$ model sufficiently predicts turbulence in both the free stream and wake, and the $k-\omega$ model more accurately predicts boundary layer separation in adverse pressure gradients near no-slip surfaces.

The spatial convective terms in Equations (9) and (10) are discretized using a second-order upwind scheme (except for pressure being solved using PRESTO! — PREssure STaggering Option, which is similar to staggered-grid schemes used on structured grids [48]) with the diffusive terms discretized using a weighted least squares cell-based construction technique. The inadequacies of the least squares approach are well-known; however, it provides accuracy that is comparable to nodal schemes [49] and due to the use of a polyhedral mesh, the least squares approach provides an adequate balance between computational expense and accuracy. The solver utilizes a pressure-based coupled approach to the equations, which is found to have superior convergence and reduced computational time than segregated algorithms [50]. The computational fluid dynamics code used in ANSYS FLUENT has been validated and used in many widespread applications, e.g., reverse flow in converging channels [51], moment and lift predictions on full-scale 3-D models of airplanes [45], bluff-body drag prediction [52], heat transfer in Couette flows [53], and complete direct injection internal combustion engine simulation [54].

Simulating the flow around a human body was found to be naturally unsteady as shown by Edge et al. [55], and the ideal approach would be solving the flow equations in a time-dependent fashion then finding the computed mean quantities manually. However, simulating the flows in a time-accurate manner and finding the computed means would be prohibitively time-consuming for this study, especially since there are a total of 18 different runs that would need to be completed. In addition to this, obtaining time-averaged results from transient simulations for all of the required runs would require computational resources beyond the capabilities of the author’s reach.⁵ Thus, the most realistic and only feasible approach was to attempt a steady-state calculation, then determine iteration-averaged quantities once a quasi-steady-state in the flow field was developed. This method is not without major drawbacks; notably, obtaining exact quantities can only be achieved by finding the limit of an infinite sample and it is therefore expected that the computed-mean will contain sampling errors. Moreover, this approach would more than likely imply that small shedding features are not resolved and thus their effects on the overall flow are ignored; this suggests that there will be accuracy implications in terms of solutions to the problems under examination.

In order to give the simulations a semblance of a fighting chance, a pseudo-transient time-stepping method was applied to the flow equations being solved. This implicit under-relaxation serves as a predictor-corrector method with the objective of fast convergence and accurate temporal integration that achieves an approximate steady state [56]. Furthermore, the use of pseudo-transient under-relaxation factors (URFs) was found to accelerate convergence in a more robust manner [57] and the rate of convergence has been shown to reassuringly arrive at a solution earlier than without the use of these URFs [58]. Hence, by taking advantage of the natural structure of the problem by evolving the

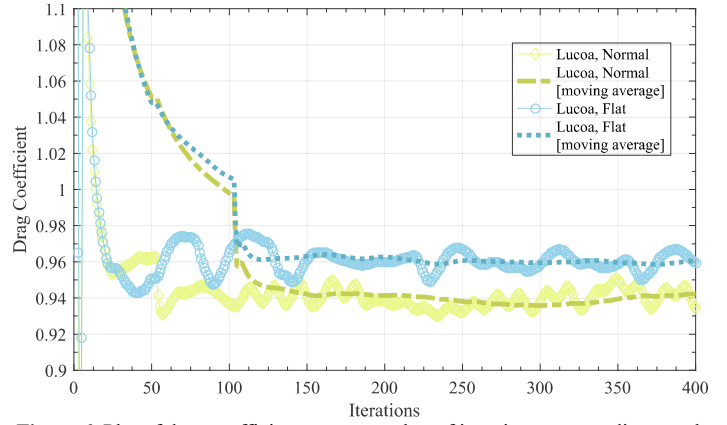


Figure 6. Plot of drag coefficient versus number of iterations on a medium mesh with an inlet velocity of $10 \text{ m}\cdot\text{s}^{-1}$.

flow equations in time, we are able to achieve a solution that reasonably integrates transient effects in a way that can be realized through the use of a steady-state calculation. In FLUENT, the pseudo time step was left to be calculated automatically following the recipe found in Section 21.6.1 of the Theory Guide [46]. This is done to hasten setup and retain consistency across all 18 simulations.

3.4 Convergence Discussion

Initial calculations were run to preview the exact behavior of the iterative calculation process; indeed, as previously demonstrated by Edge et al., the inherent unsteadiness of the flow resulted in difficulties obtaining reduced residuals, with the scaled continuity residuals hovering below but near $1\cdot 10^{-2}$, and other residuals remaining below $1\cdot 10^{-4}$. A technique stemming from experience was devised to assist in reducing the residuals while maintaining spatial accuracy. For the first 50 iterations, a blending method between first and second order spatial discretization schemes (with a bias for the first order scheme), lower URFs, and an “aggressive” pseudo-time step, were used to rapidly approach a quasi-stable solution. The following 100 iterations switched the spatial discretization scheme to a higher order method along with raised URFs to increase accuracy. The remaining iterations were then run using a “conservative” pseudo-time step scaled by 0.5 to further converge and resolve flow details that are more apparent on a smaller timescale. This technique enabled the residuals to drop by nearly an order of magnitude, and thus it was used for all other simulations.

As discussed in Section 3.3, taking mean quantities of a finite sample will incur sampling errors of which are difficult to quantify compared to a mean derived from an infinite sample. However, a potential approach to help determine the exact nature of these errors would be taking an integrated surface quantity, such as drag coefficient, and seeing how this quantity changes as the iterations progress. Such a measure serves as an observed global variable in that the measured quantity is dependent on how accurate the grid can resolve the flow. Figure 6 shows the iteration history of drag coefficient between the two models taken with an inlet velocity of $10 \text{ m}\cdot\text{s}^{-1}$ and run using a grid with medium refinement (refer to Section 3.5 for refinement details). The figure shows that the solution reaches quasi steady-state values after 150 iterations, with an oscillatory period occurring roughly every 140~150 iterations. A 100 iteration moving average calculated by FLUENT was applied to the values to assist in determining if overall convergence was reached. Looking at the tendency of the averages, it is reasonable to conclude that the solution is indeed quasi-stable. With the average varying very little compared to actual iteration values, and for the sake of minimizing computational expense in this study, this observed tendency incurs a reasonable assurance that the simulations are adequately converged. Finally, the net flux imbalance was calculated to be less than 1% of the smallest flux through the domain, further supporting convergence [59].

⁵ The astute reader should note that for all of the simulations, a laptop using 2011-era hardware (Intel i7-2820QM processor, 16 GB RAM) was used.

3.5 Numerical Uncertainty and Grid Selection

Moving forward, to preserve accuracy and to assure low computational costs, the effect of grid resolution is studied by comparing results on drag coefficient using different grids of different refinement. The importance of grid convergence and examination of discretization errors in CFD simulations have been demonstrated across numerous organizations [60, 61] and journals [62], and the necessity of quantifying these errors have led to well-established methods that attempt to describe effects of resolution to that of the extrapolated solution [63]. Although it has been repeated in this paper that quantifying exact errors is essentially a fruitless adventure, the additional time spent on understanding the potential discretization error nonetheless is useful in helping select a grid that balances the required resolution to minimal processing power.

In this grid refinement study, each model used three different grids that are refined methodologically by decreasing the cell spacing within the BOIs. Between both models, the grid generation methods remained the same and follows the procedures as described in Section 3.2. Representing fine (grid 1), medium (grid 2), and coarse (grid 3) respectively, the Normal model utilized grids containing $2.82 \cdot 10^6$, $2.32 \cdot 10^6$, and $1.53 \cdot 10^6$ elements. The Flat model used $2.67 \cdot 10^6$, $2.16 \cdot 10^6$, and $1.41 \cdot 10^6$ elements. The difference in overall element counts are attributed to the reduced surface area of the Flat model compared to the Normal one. For sake of completeness and following the method as recommended by The American Society of Mechanical Engineers [64], the subsequent equations are presented to determine the discretization error between the described meshes. Letting h denote the representative grid size,

$$h = \left[\frac{1}{N} \sum_{i=1}^N (\Delta V_i) \right]^{1/3} \quad (11)$$

where ΔV_i is the volume of each cell. Let $h_1 < h_2 < h_3$ and let r designate the refinement ratio between successive grids, such that $r_{21} = h_2/h_1$ and $r_{32} = h_3/h_2$. Calculating the apparent order of accuracy, p , involves solving the following expression using a fixed-point iteration and using the first term as the initial guess:

$$p = \frac{1}{\ln(r_{21})} \left| \ln|\epsilon_{32}/\epsilon_{21}| + \ln \left(\frac{r_{21}^p - s}{r_{32}^p - s} \right) \right| \quad (12)$$

where $s = \text{sign}(\epsilon_{32}/\epsilon_{21})$, $\epsilon_{32} = \phi_3 - \phi_2$, $\epsilon_{21} = \phi_2 - \phi_1$, and ϕ_i representing the quantity being investigated. Finding the extrapolated, asymptotic value involves calculating

$$\phi_{ext}^{21} = (r_{21}^p \phi_1 - \phi_2) / (r_{21}^p - 1) \quad (13)$$

with ϕ_{ext}^{32} being similar. Then, the following error estimates can be found:

$$e_a^{21} = \left| \frac{\phi_1 - \phi_2}{\phi_1} \right| \quad (14)$$

$$e_{ext}^{21} = \left| \frac{\phi_{ext}^{21} - \phi_1}{\phi_{ext}^{21}} \right| \quad (15)$$

$$\text{GCI}_{21} = \frac{1.25 e_a^{21}}{r_{21}^p - 1} \quad (16)$$

with e_a^{21} describing the approximate relative error, e_{ext}^{21} describing the extrapolated relative error, and GCI_{21} being the grid convergence index (GCI). e_a^{32} , e_{ext}^{32} , and GCI_{32} are calculated similarly.

The GCI is an indicator with a 95% confidence interval of how far the finer of the two compared grids is to the asymptotic value ϕ_{ext} and predicts how further refinement affects the solution [65]. The evaluated quantities are taken after 400 iterations, which in Figure 6 and discussed previously, has shown to provide a reasonable amount of iterations to

determine a sufficiently averaged quantity. The results from the previous equations are summarized in Table 2.

Table 2. Grid summary and calculations of discretization error between the two models.

$\phi = \text{drag coefficient at } 10 \text{ m}\cdot\text{s}^{-1}$	Lucoa, Normal	Lucoa, Flat
N_1, N_2, N_3	$2.82 \cdot 10^6, 2.32 \cdot 10^6,$ $1.53 \cdot 10^6$	$2.67 \cdot 10^6, 2.16 \cdot 10^6,$ $1.41 \cdot 10^6$
Average wall clock time per 100 iterations (minutes)	72, 38, 19	67, 34, 17
Average memory usage per compute thread (MB)	1674, 985, 648	1546, 916, 542
h_1, h_2, h_3	0.025541, 0.027221, 0.031327	0.026007, 0.027912, 0.032206
ϕ_1, ϕ_2, ϕ_3	0.9352, 0.9418, 1.0015	0.9501, 0.9581, 1.0178
r_{21}, r_{32}	1.06577, 1.15083	1.07325, 1.15384
$\epsilon_{21}, \epsilon_{32}$	0.00659, 0.09700	0.00798, 0.05974
p	12.8180	11.4372
$\phi_{ext}^{21}, \phi_{ext}^{32}$	0.9299, 0.9299	0.9437, 0.9437
e_a^{21}, e_a^{32}	0.70%, 6.34%	0.84%, 6.24%
$e_{ext}^{21}, e_{ext}^{32}$	0.56%, 1.27%	0.68%, 1.53%
$\text{GCI}_{21}, \text{GCI}_{32}$	0.70%, 1.57%	0.84%, 1.88%

All grids were noted to converge in a monotonic manner, indicating the average flow field certainly benefits from grid refinement. As shown by the lower values of GCI_{21} to that of GCI_{32} , it would be most beneficial to run all the simulations using the fine grid. On the other hand, as accuracy increases, so do memory and compute requirements. The finest grid managed to exceed the available physical memory on the machine that the simulations were run on. In addition, calculations were found to require nearly double the amount of time to arrive at a solution compared to the medium grid. The tradeoff between the reduction in GCI and resource consumption was too great considering the limited resources to begin with and the potential amount of time required for all 18 simulations. Therefore, as shown from this grid study, the medium grid serves as the most practical balance between accuracy and resource expenditure; for all simulations, the medium grid was selected.

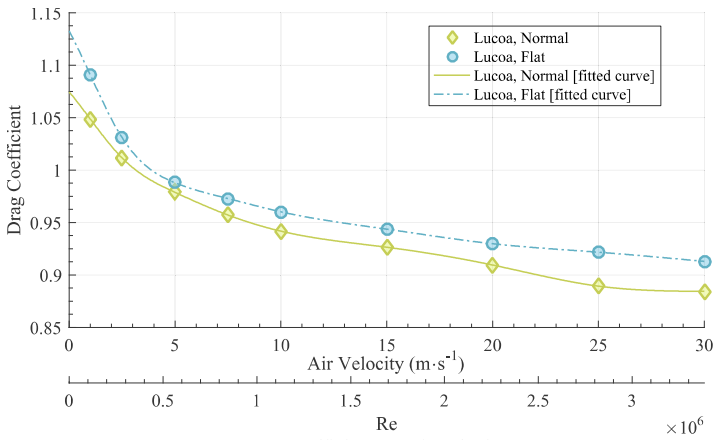
4. Results and Discussion

The immediate discrepancies between Lucoa's model and other human models used in similar studies (other than the fact that she has an enormous chest) are the presence of horns, a baseball cap, raised arms, and solidly modeled hair. Each affects the wake in their respective manner, with these individual effects being described in the following subsections. It is important to recognize that although these differences between Lucoa and other human models are present, they nonetheless do not affect the direct comparison between the Normal and Flat models, which was a primary objective of this work.

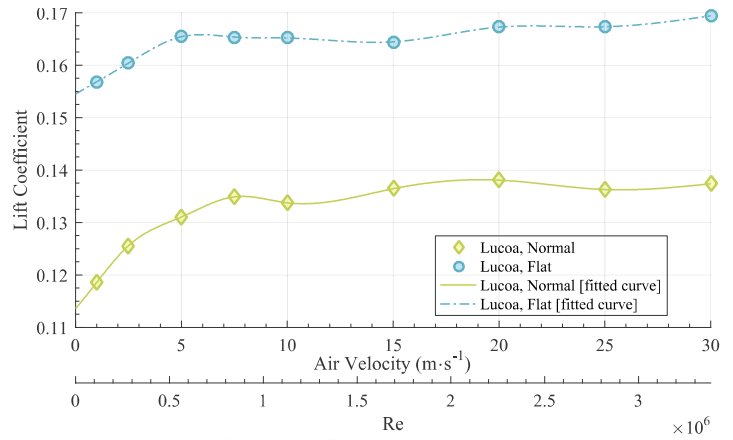
The following subsection details the variances of drag and lift as air velocity changes and compares the outcomes to previous studies on the human form. The subsequent subsections delve into the differences in wake structure through the analysis of streamlines, velocities, TKE, and skin friction. While no sound comments can be made on the concise form of instantaneous flow structures, quasi steady-state general features present in the flow are described.

4.1 Velocity-Based Trends

The convergence method presented in Section 3.4 was used for all velocities listed in Table 1 between the two models. The drag and lift were calculated using the same 100 iteration moving average in FLUENT and the values at the end of 400 iterations were used. Figures 7-9 plot the results between the two models. In all of the figures, a cubic spline was used to interpolate the data. The figures labeled with "(a)" correspond to drag-related values while figures labeled with "(b)" correspond to lift-related values.

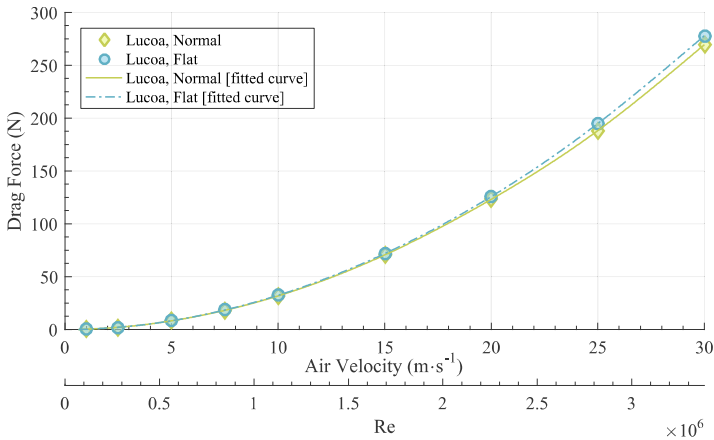


(a) Drag coefficient vs. air velocity.

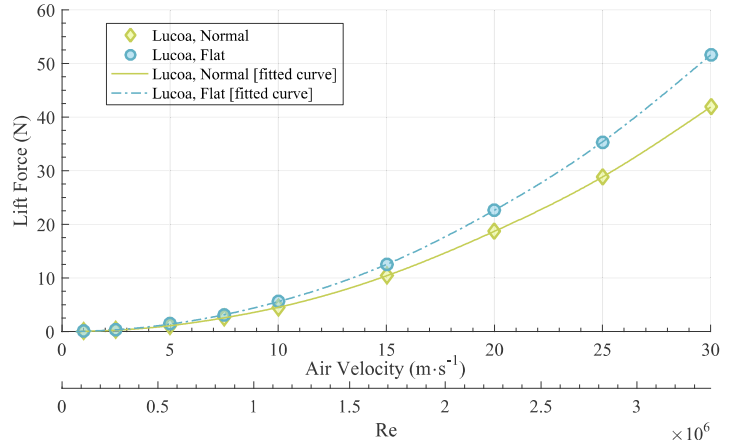


(b) Lift coefficient vs. air velocity.

Figure 7. Plots comparing coefficient quantities between the two models.

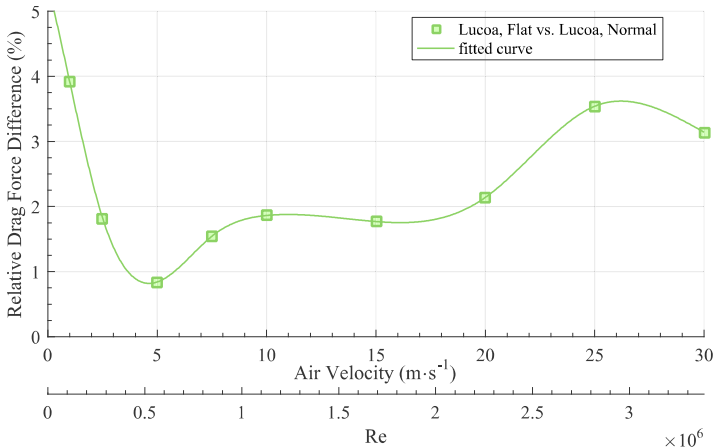


(a) Drag force vs. air velocity.

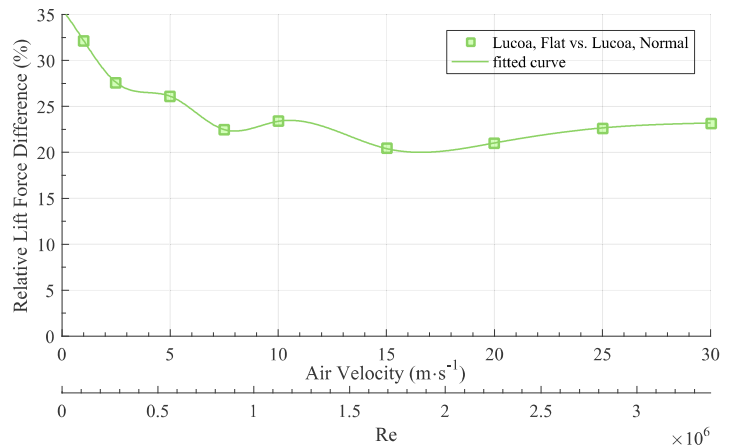


(b) Lift force vs. air velocity.

Figure 8. Plots comparing the forces experienced on the two models at various air velocities.



(a) Relative drag difference of the Flat model to the Normal model.



(b) Relative lift difference of the Flat model to the Normal model.

Figure 9. Plots indicating the relative force differences of the Flat model compared to the Normal model.

Figure 7 focuses on the coefficients, and it is readily apparent that at all velocities, the Flat model incurs higher coefficients than the Normal model. In the region near $5 \text{ m}\cdot\text{s}^{-1}$, the drag coefficients between the two models were closest to one another. Judging from the errors described in Section 3.5, it is safe to presume that these differences are within the error bounds and therefore the difference between the two models near this velocity is negligible. In 7(a), it is interesting to observe that the drag coefficients decrease following a power relation corresponding to velocity. This relation most likely arises from the peculiarity of the solidly modeled hair; downwash due to the hair diverts air behind the torso then directs the air downwards, which causes less air to flow directly behind the body. Presumably, this downwash closes off the size of the primary recirculation region (PRR) behind the body.

As the air velocity increases, the effect of the downwash becomes more prominent and therefore a general decrease in the drag coefficient is observed. The large breasts on the Normal model may also play a role in enhancing this downwash effect, as the air is gradually diverted around the bust and is able to maintain momentum before being redirected by the hair. The stronger resulting downward jet of air thus closes off the recirculation region more effectively. The degree of which this downwash affects drag is difficult to determine from this study, but it is reasonable to deduce that due to the drag reduction of the Normal model compared to the Flat model, the effects are markedly noticeable. The geometrical presence of the breasts may also have an effect in reducing drag as they smoothly redirect a portion of the air around the torso,

whereas the Flat model simply forces majority of the air to stagnate at the chest, which incurs higher drag.

The difference in lift is notably more dramatic than drag. In [Figure 7\(b\)](#), the lift coefficient for both models gradually increases from 1 to $10 \text{ m}\cdot\text{s}^{-1}$ then levels off as the velocity changes. This increase can also be contributed to the downwash from the hair, since as the velocity increases, there is a higher flow rate and thus more fluid mass pushing upwards against the models. The brim of the baseball cap on both models may additionally contribute to lift as it lies orthogonal to the mean flow direction and causes a buildup in pressure in front of the face. The Normal model provides a lower lift coefficient possibly due to the breasts providing downforce; since the Normal model has a significant and primarily upward sloping surface in front of the torso that the Flat model lacks, the downward force from the air flowing atop the bust most likely provides this reduction in lift. Granted, due to the geometry being modeled as completely solid, this effect does not account for breast deflection caused by these forces. Nonetheless, the presence of Lucoa's large breasts evidently provides a reduction in lift.

[Figure 8](#) provides a comparison of the actual forces experienced on the models. As seen in both [8\(a\)](#) and [8\(b\)](#), the forces increase following a roughly squared relation, which is what would be expected looking at the velocity relationship in [Equations \(1\)](#) and [\(5\)](#). As elaborated in the previous paragraphs, the difference in drag is less dramatic than that of lift, and this is reflected by the more difficult to discern plots in [8\(a\)](#) than in [8\(b\)](#). This observation is further expanded upon in [Figure 9](#), which compares the relative force difference the Flat model encounters compared to the Normal model. Looking at [9\(a\)](#), the Flat model experiences a nearly 4% increase in drag at $1 \text{ m}\cdot\text{s}^{-1}$, however, this value decreases immediately and falls to below 1% at $5 \text{ m}\cdot\text{s}^{-1}$. From 5 to $10 \text{ m}\cdot\text{s}^{-1}$, the difference between the two widens again, levels off from 10 to $20 \text{ m}\cdot\text{s}^{-1}$, then impetuously increases at $25 \text{ m}\cdot\text{s}^{-1}$ and remains markedly greater at the highest tested velocity of $30 \text{ m}\cdot\text{s}^{-1}$. The reason as to why the drag difference reaches its minima at $5 \text{ m}\cdot\text{s}^{-1}$ cannot be directly inferred from this work. Throughout the tested velocity range, the Flat model incurs an average drag increase of 2%, which, in the context of day-to-day life at low air velocities, is practically insignificant. However, in regards to performance, the large breasts on the Normal model can prove to be advantageous, assuming the overall position remains similar to the erect postures of the models. The degree of which this advantage can be quantified depends heavily on the type and duration of competition to be examined, which is not discussed further in detail. The relative lift force difference averages 24%, with the values ranging from 32% at $1 \text{ m}\cdot\text{s}^{-1}$, gradually decreasing to 21% near $15 \text{ m}\cdot\text{s}^{-1}$, and then slightly increasing to 23% at the highest tested velocity. From this result, the presumed effect of Lucoa's breasts reducing lift is more pronounced at lower air velocities, while still remaining effective as the velocity increases.

Table 3. Comparisons of drag coefficient with other researchers' results.

Researchers	Year	Reference	Posture	C_D
This study	-	-	Standing (Normal model)	$0.89 \sim 1.05$
			Standing (Flat model)	$0.91 \sim 1.09$
Hill	1927	[1]	Standing	0.98
Schmitt	1954	[7]	Standing (clothed)	Approx. 1.36
			Standing (nude)	Approx. 1.20
Shanebrook and Jaszczak	1976	[66]	Running (cylindrical model)	1.2
Penwarden et al.	1977	[67]	Standing (clothed)	1.18
Davies	1980	[2]	Running	0.87
Brownlie et al.	1987	[68]	Standing	$0.96 \sim 0.98$
Gómez et al.	2013	[69]	Running	1.20
Inoue et al.	2016	[70]	Running (without ground effects)	1.17

[Table 3](#) summarizes the encountered drag that both models experienced throughout the tested velocity range, together with other researchers' experiments. As a result, the present study reveals that Lucoa's form tends to correspond favorably to experiments done with standing models. It is seen that Lucoa's results overlap with those of Hill [1] and Brownlie et al. [68]. Schmitt's [7] results were an atypical case as the drag coefficients in that study were based on the entire surface area of the body divided by the product of volume and subject height, instead of the customary frontal projected area used elsewhere. This resulted in coefficients ranging from 10 to 13, necessitating a recalculation in order to more directly compare to the other results in [Table 3](#). It was demonstrated through Schmitt's results that the use of nude subjects (akin to having smooth walls as mentioned in [Section 3.1](#)) result in lower drag. Although the values for nude subjects were still greater than those found in the current study, this finding provides additional support as to why Lucoa's overall form tends to encounter lower coefficients in contrast to other studies. With the objective of obtaining C_D values for a wide range of people in everyday situations, work done by Penwarden et al. [67] confirms that clothing certainly increases drag. Furthermore, the authors in that study comment that extrapolating their data to simulate bare-skinned models would result in values more akin to that of Hill's data, thereby supporting the notion that Lucoa's results are indeed realistic.

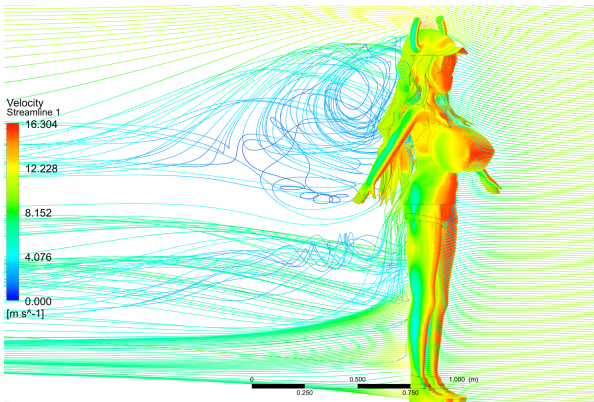
Comparisons to results based around running are also provided, as this form of competition is a natural progression from simply standing. Understandably, a runner will experience higher drag due to their ever-changing position and the strict anti-symmetry in orientation. Shanebrook & Jaszczak [66] investigated drag through the use of a generalized cylindrical human model, analogous to the assumptions described in [Section 1.1](#). As such, their results parallel those of other investigations done on runners and show that a cylindrical model can provide convincing data. Davies' [2] work discovered that the effects of Reynolds number remained constant below velocities of approximately $18 \text{ m}\cdot\text{s}^{-1}$. Conversely, this effect was not seen in this study, which most likely harkens back to the drawback of the modeled hair. Gómez et al. [69] developed a parametric model of drag that considered both velocity, u , and acceleration, u^2 , based on the record-setting performance of Usain Bolt. They revealed that 92% of energy used in running is absorbed by drag, which bolsters both the significance of the drag reduction and the implicational anthropomorphic advantage that Lucoa has. Inoue et al. [70] examined the effects of a moving belt system to simulate ground effects of a runner, in addition to providing data on how leg position (e.g., forward or behind) changes drag. From their study, it was observed that having the legs placed either forward and behind veritably increases drag due to the posture. Consequently, it is expected that a prospective study incorporating the effects of running based on the present results (as described in herein and [Table 3](#)) would feature comparable C_D values. While the current stationary results may not be directly applicable to the moving case, they nevertheless offer a suitable starting point on which to base further research.

4.2 Salient Flow Analysis

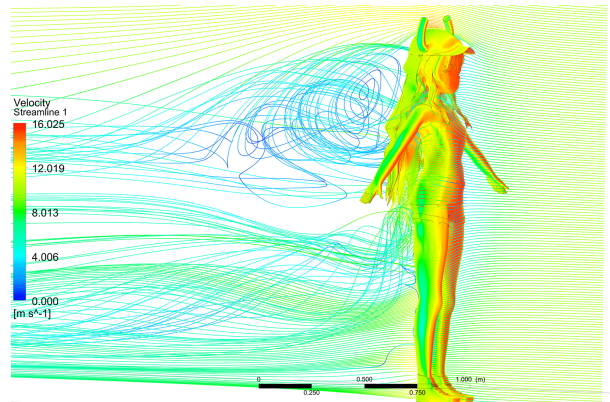
Discussion pertaining to the variances in flow structures is examined under an air velocity of $10 \text{ m}\cdot\text{s}^{-1}$. In addition to being previously examined in [Sections 3.4](#) and [3.5](#), this velocity is readily achievable under human locomotion [69], making the selection straightforward. While the results are derived from a quasi-steady-state approach, general flow structures can be reasonably interpreted.

4.2.1 Streamlines and Flow Velocities

As reflected in [Figures 10-13](#), the fluid dynamics of the wake are shown with the use of streamlines colored according to velocity magnitude. The figures labeled as "(a)" and "(b)" correspond to the Normal and Flat models respectively. The overall wake structures revealed in [Figure 10](#) fall into two distinct regions based on height, with the PRR found above the hips and extending to the top of the head, and a second, more complex regime behind the legs. The works described in [Section 1.1](#) correctly predicted these structures. Specifically, the PRR for both

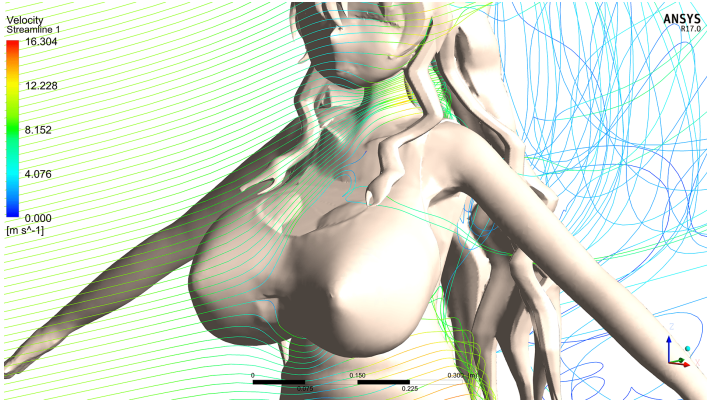


(a) Wake structures associated with the Normal model.

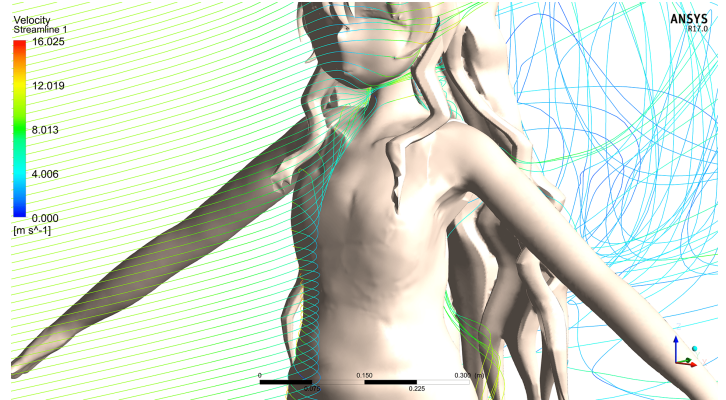


(b) Wake structures associated with the Flat model.

Figure 10. Streamlines emanating at $x = 0$ and spanning a line from $0 \leq z \leq 2.3$ meters showing primary flow structures. Pressure experienced on the models is also shown.

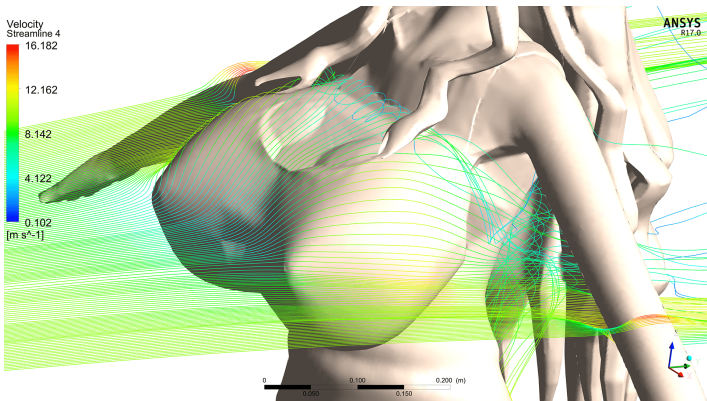


(a) Set of vertically aligned streamlines on the Normal model.

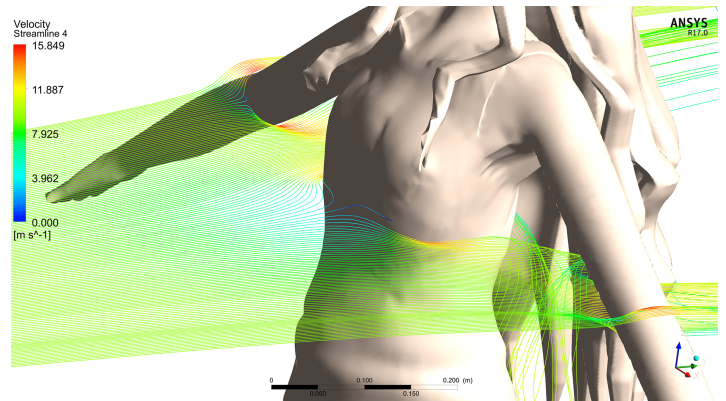


(b) Set of vertically aligned streamlines on the Flat model.

Figure 11. Detailed view of flow structures around the chest of the models using the same streamlines from Figure 10.

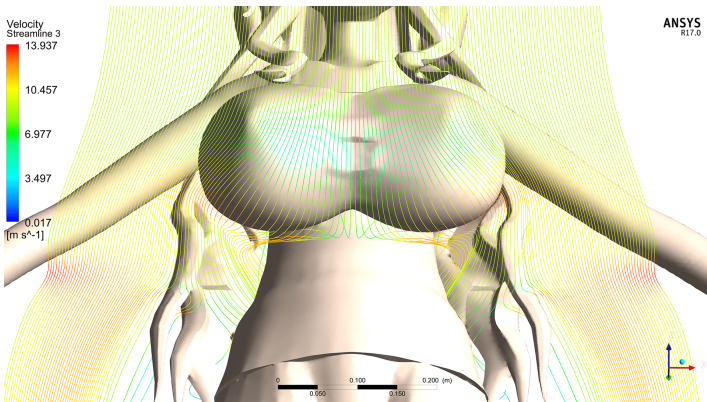


(a) Set of horizontal streamlines on the Normal model flowing atop the bust.

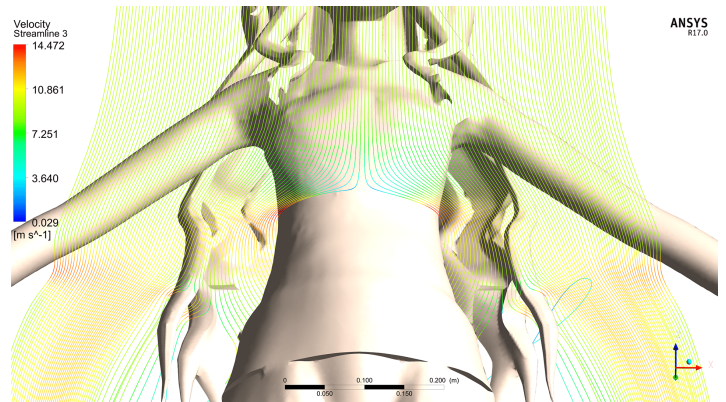


(b) Set of horizontal streamlines on the Flat model at the same z -location.

Figure 12. Detailed view of flow structures around the chest using streamlines emanating at $z = 1.18$ meters and spanning a line from $-0.5 \leq x \leq 0.5$ meters.



(a) Set of horizontal streamlines on the Normal model flowing beneath the bust.



(b) Set of horizontal streamlines on the Flat model at the same z -location.

Figure 13. Detailed view of flow structures around the chest using streamlines emanating at $z = 1.14$ meters and spanning a line from $-0.5 \leq x \leq 0.5$ meters.

models was found to extend roughly 1.4 meters downstream, or approximately 4 times the width of the torso, which agrees strongly with Okamoto's and Sunabashiri's findings. The type of vortex shedding in this recirculation region cannot be determined, but it is expected to nonetheless be asymmetric, with the large-scale structures being advected downstream based on the findings of Edge et al. The wake behavior behind the legs were also discovered to obey the findings summarized by Zhou and Alam, with the region from the ankles to the knees having wake structures associated with each leg, and the region from the knees to the hips behaving as a unified bluff-body. The figure also shows a distinct vertical "jet sheet" stemming from the gap between the legs, with an average magnitude approximately 35% greater than the free stream velocity. A vortex pair originating from the top of the legs is also evident. This vortex pair can be seen being caused by the downwash of the hair; the momentum of the downward flow interacts with the air flowing past the top of the thighs, which results in these prominent structures. Additional momentum provided by the jet of air between the legs further enhances the strength of these vortices. Furthermore, the effects of the downwash are evident in the way the vortex pair assumes a downward angle as the flow advects; this is indicative of the significant amount of air being captured by the geometry of the hair.

From what can be drawn from comparing Figure 10(a) and 10(b), the Flat model has a weaker, less organized vortex stemming from the legs. This observation may further explain why the Normal model has lower lift than the Flat model. Aider et al. [71] described the effect of vortex pairs affecting lift and drag, and shown that inflow caused by streamwise counter-rotating vortices result in a net downward force. Thus, the weaker vortex pair on the Flat model contributes less towards reducing lift than the Normal model. Following this, it is reasonable to suggest that the behavior of the drag curve in Figure 7(a) can be attributed to the formation of these vortices; the energy being redirected into the formation of these structures diverts a portion of the mean flow away from the PRR, leading to drag reduction as the velocity increases.

Figure 11 provides a close-up look at the same streamlines in Figure 10 around the torso of both models. As can be seen in 11(a) and correctly determined in Section 4.1, the breasts provide a gradual interface for the air to move around the torso compared to the relatively abrupt obstruction the Flat model imposes as reflected in 11(b). This is further exemplified in Figure 12, which shows a set of horizontal streamlines positioned at $z=1.18\text{m}$. In 12(a), the air flows smoothly atop the breasts at a velocity approximately 40% to 60% of the free stream velocity, whereas the Flat model in 12(b) simply forces a relatively larger portion of the incoming air to stall at the torso. It is interesting to note that a small recirculation region develops directly atop the breasts, which most likely is dependent on the angle between them and the chest. From what can be seen in 12(a), this small recirculation region prevents a small portion of air from surmounting the shoulders and instead redirects the air downwards and off to the sides of the torso. Figure 13 provides an upwards facing view of the models along with horizontal streamlines emanating from $z=1.14\text{m}$. In 13(a), air flowing beneath the bust gains a velocity that is approximately 20% higher than the mean free stream velocity before being diverted perpendicular to the body and interacting with the incoming air stream and the rest of the torso. By the action of the breasts, the air is diverted in such a way that it is able to maintain momentum while it moves around the rest of the chest. This is in contrast to 13(b), where a portion of the air is forced to stall in front of the chest before being redirected around the torso, much like as was seen in other figures involving streamlines with the Flat model.

Figure 14 compares the velocity magnitude of the wake behind the two models at five different z -locations. At these locations, data is sampled along a line centered at the midline ($x=0$) and spans downstream from $-1 \leq y \leq 2$ meters. The z -locations are taken at heights of $z = 0.1\text{m}$, $z = 0.5\text{m}$, $z = 0.9\text{m}$, $z = 1.18\text{m}$, and $z = 1.55\text{m}$, all of which correspond to the feet, legs, hips, chest, and head, respectively. From this comparison, the differences in wake velocities are slight, with the only significant difference occurring at the height of the legs. At this height, it can be seen that the Flat model has a wake velocity that is consistently higher than that of the Normal model. This observation can be attributed by the lower energy present in the vortices generated by the Flat model;

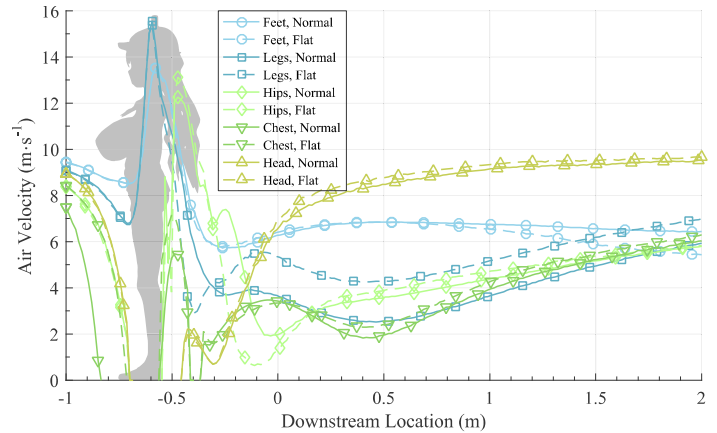


Figure 14. Comparison of wake velocity magnitudes at 5 z -locations centered along $x = 0$ and ranging from $-1 \leq y \leq 2$ meters. Lucoa positioned and to scale with x -axis.

Feet $z = 0.1\text{m}$, Legs $z = 0.5\text{m}$, Hips $z = 0.9\text{m}$, Chest $z = 1.18\text{m}$, Head $z = 1.55\text{m}$.

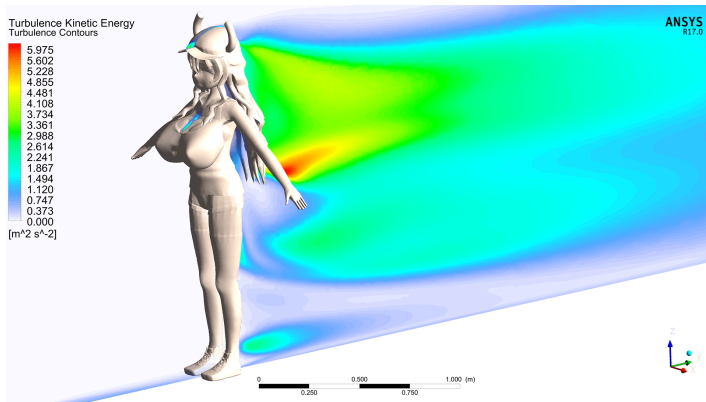
these weaker formations are affected by the mean flow to a greater degree and thus the velocity magnitude in this region is higher than if the vortices were to have greater strength, as seen with the Normal model.

4.2.2 Turbulence Kinetic Energy

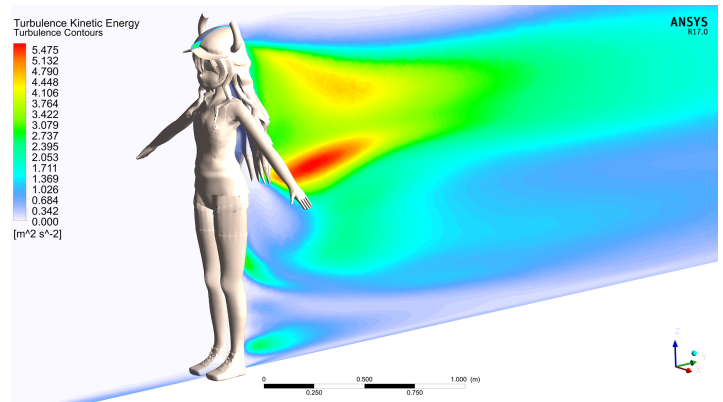
Figure 15 shows a slice of the domain through the median plane of the models, indicating the TKE present in the flow. At first glance, contours for both models present the same general structures as described earlier, such as the PRR behind the torso and the smaller structures associated with the legs. Due to the automatic scaling of the colors, the differences present in the PRR of the Flat model compared to the Normal model are slightly exaggerated. However, the differences are still distinguishable in that the PRR for the Flat model has a measurably higher level of TKE than that of the Normal model. Indeed, 15(b) indicates that the two apparent bands of significant TKE associated with the PRR are generally more intense, even after factoring the differences between the color scales. Common to both models is a region behind the hips where the relatively highest TKE was measured. This lower band within the PRR was found to be more compact for the Normal model, whereas the Flat model had a marginally less intense and more widespread band. This effect may be attributed to the way the downwash from the hair interacts with the PRR.

Directly below the PRR is the TKE present in the vortex pairs originating from the legs. In 15(a), the Normal model has a notably higher level of TKE associated with these vortices, coupled with the observation that this energy is maintained as the flow advects downstream. In contrast, 15(b) shows that the TKE in the vortices is lower and that the energy is dissipated sooner. This remark further supports the interpretations hitherto; that the formation of stronger vortices the Normal model generates plays a role in reducing both drag and lift by diverting energy away from the PRR.

Smaller regions with notable TKE present between both models are those associated directly behind the legs, at the ankles, and directly above the brim of the baseball cap. Between the two, the TKE at the ankles remains unperturbed by the differences in the wake structures above it. This region is related to the individual wakes associated with each foot, behaving much like the two cylinder arrangement as described earlier. A downward "jet" of TKE originating from the thighs and curling parallel to the mean flow direction at the height of the knees shows some variability between the two models. This region is linked to the "jet" of air that is formed between the legs interacting with the downwash from the hair. With the Normal model in 15(a), this "jet" of turbulence remains both vertical and closer to the legs. In 15(b), this region takes on a slightly more horizontal transition and extends farther into the wake. A small recirculation region, much like that associated with the breasts on the Normal model, is found above the brim of the baseball cap, which is due to the blunt transition the shape of the head imposes to the incoming flow.

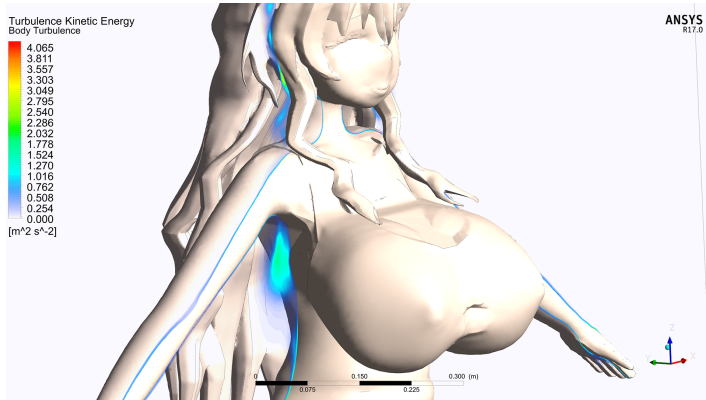


(a) TKE associated with the Normal model.

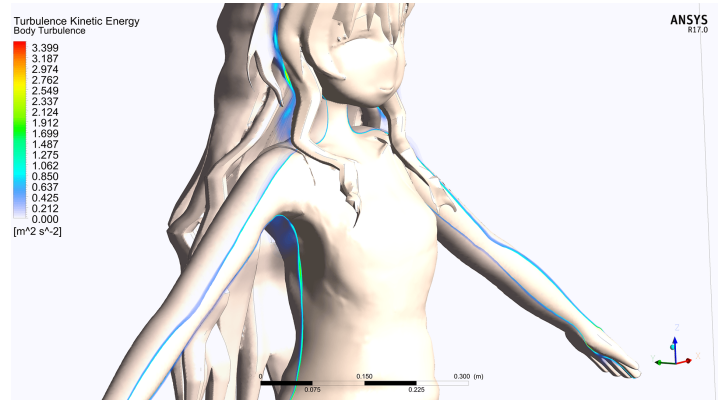


(b) TKE associated with the Flat model.

Figure 15. TKE present in the flow behind the models along the median plane.



(a) TKE present behind the breasts of the Normal model.



(b) TKE present around the torso of the Flat model.

Figure 16. TKE present around the torso of both models along the coronal plane.

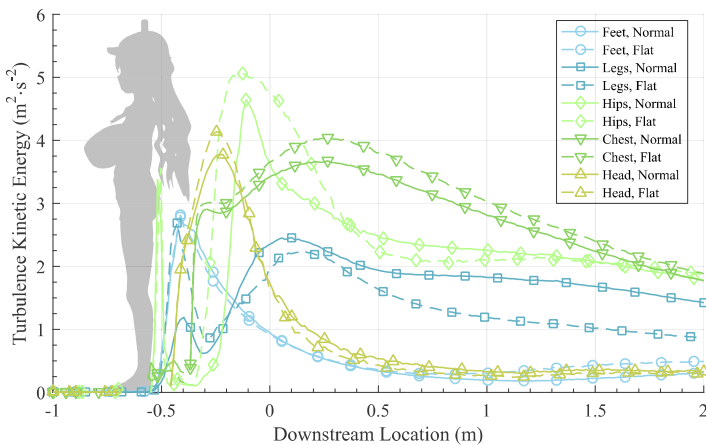


Figure 17. Comparison of TKE at 5 z-locations centered along $x = 0$ and ranging from $-1 \leq y \leq 2$ meters. Lucoa positioned and to scale with x-axis. Feet $z = 0.1\text{m}$, Legs $z = 0.5\text{m}$, Hips $z = 0.9\text{m}$, Chest $z = 1.18\text{m}$, Head $z = 1.55\text{m}$.

Figure 16 shows the TKE around the torso of both models along the coronal plane. As obvious as the difference between both models, the presence of a turbulent region behind the breasts and below the axilla comes as no surprise. It is apparent that this region is influenced by the small recirculation region that forms above the breasts spilling air downwards and behind the torso, which can be seen in Figure 12(a). Furthermore, air from beneath the breasts also contributes to the size of this region, as in Figure 13(a) it can be understood that this layer of accelerated air provides additional shear against the flow from above and increases the turbulence behind the breasts. Since the Flat model lacks such features, Figure 16(b) presents an understandably unremarkable result, with only a small sliver of turbulence along the side of the torso. Common to both models however, is turbulence being generated by the hair itself, stemming from the hair being left modeled as solid. The true extent of how much turbulence is generated from the solid hair and its effects on the PRR is unfortunately intractable from this current

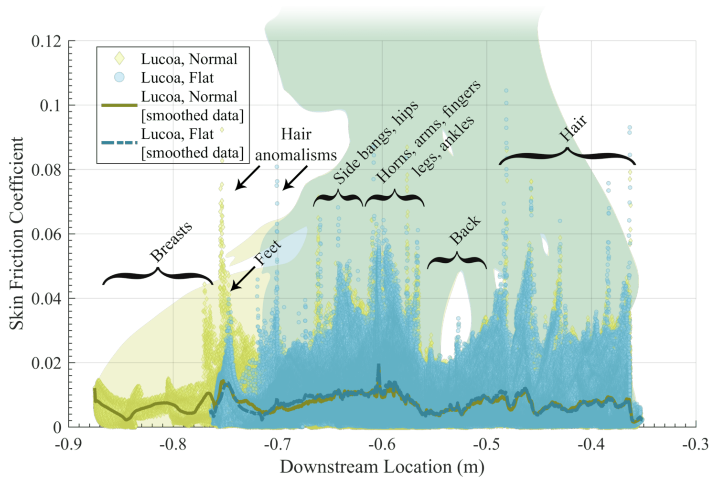
study due to its highly complex geometry. Though, it is expected that simulations dealing with physically accurate hair may undoubtedly increase turbulence, and hence, drag, based on casual observations done on how hairstyles can affect aerodynamic performance [72].

The same approach used to obtain information as seen in Figure 14 was used in Figure 17, with TKE being measured instead of velocity. As indicated from this figure, it is seen that the vortices originating from the legs indubitably diverts energy away from the PRR and supports the findings stemming from Figure 15. This is reflected with stronger overall turbulence present at z-locations corresponding with the hips, chest, and head for the Flat model, along with markedly lower TKE at the level of the legs in contrast to the Normal model. Slight differences are noted, with the Flat model having a higher peak TKE at the legs immediately behind the body than the Normal model. Then, from 1 to 2 meters downstream, the Normal model generates a greater amount of TKE. This observation may ultimately be attributed to the difference in shape the leg vortices assume between the two models.

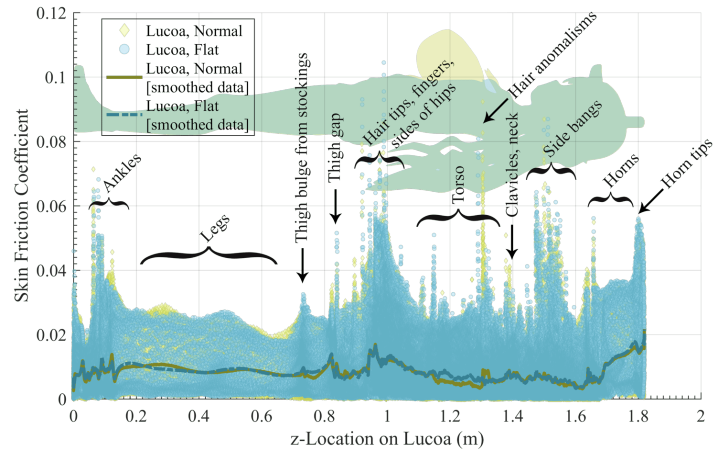
4.2.3 Skin Friction Coefficient

An evaluation of the effects of the macroscopic geometry between the two models on skin friction is shown with Figure 18. This figure represents a scatter plot of C_f measured at every vertex on the models, with regions of relatively high C_f labeled according to which location on the model they are found on. Two directions are evaluated, with the x-axis on 18(a) representing the streamwise position, and the x-axis on 18(b) representing the z-location. A silhouette of the models present in the background of the plots are positioned and scaled to their respective x-axis to further provide context with the labeling. Additionally, the data was averaged and plotted along with the scatter plot to reveal discrepancies that may be more difficult to discern.

Expectedly, both models feature the same general scatter plots, with nearly negligible differences. However, common to both models and the plots are the presence of numerous spikes associated with the hair. Inasmuch as they are an artifact of the hair being modeled solidly, these spikes are aptly denoted as “hair anomalisms” within the plots. As such,



(a) Skin friction of both models sampled along the streamwise direction.



(b) Skin friction of both models sampled along the z-direction.

Figure 18. Scatter plots of skin friction comparing both models. Sources of regionally significant C_f are labeled. An additional plot denoting a smoothed average of the scatter data is present to provide clarity in comparison. Silhouettes of the models are positioned and scaled according to their respective axis in the plots.

the hair is undeniably a major contributor to skin friction on the models. This is especially apparent in 18(a), with the source of skin friction being contributed solely by the hair from the rear of the model. Another exemplification of the hair’s effect on C_f can be seen in 18(b), with a grouping of peaks obtaining a value of 0.06 corresponding to the hair tips and bangs around the face. Additional sources of significant C_f can be easily observed in the same figure, such as the ankles, around the thighs, the fingertips, and especially Lucoa’s horns. These dramatic changes to skin friction indicate where on the models flow separation is more likely to occur, which in turn, relates to where turbulence can potentially be generated.

The breasts, compared to the relatively noisy scatter generated by the rest of the body, provides a smooth transition in regards to skin friction over its surface. A small spike found at the downstream location of $y = -0.77\text{m}$ in 18(a) corresponds to the small recirculation region above the breasts seen in Figure 15(a). In a sense, it can be deduced that the breasts act to reduce C_f , which can be seen as a small dip in the smoothed data centered around $z = 1.2\text{m}$ in 18(b). However, even with such a diverse of a plot, the average C_f across the whole body can be seen as roughly 0.01 from both figures, which indicates how little skin friction actually affects overall drag with bluff bodies.

5. Summary and Recommendations

This paper has offered a unique compendium of data providing insight into the effects of a specific physiological feature on the aerodynamic performance of a human. As such, the results have indicated that large breasts can be notably aerodynamic through the reduction of drag and lift. The Flat model incurred a 4% maximum drag increase compared to the Normal model, with an average of approximately 2% spanning velocities from 1 to 30 $\text{m}\cdot\text{s}^{-1}$. The Flat model also experienced more lift, with a maximum difference being 32% and averaging 22%. As illustrated, the mechanism behind the drag and lift behaviors observed between both models was elucidated through the analysis of streamlines around the body and the structures associated with TKE; the Normal model provides advantageously lower drag and lift by the generation of stronger vortices from the legs, which in turn originates from the action of the breasts redirecting the flow around the torso. From what has been presented in this preliminary work, it is safe to conclude that the phrase “Flat is Justice” is deficient aerodynamically.

A major shortcoming intrinsic to this study was the decision to leave the hair present in the models as immovable and solid. As noted earlier, a significant portion of the air flowing around the body was captured by the geometry of the hair, and this affected the wake structures behind the model. This effect therefore blunts the overall applicability of the results found in this study to actual human models. It is important to note, however, that large breasts do give a consistently notable aerodynamic advantage, as reflected in the overall lower forces

experienced by the Normal model. Additionally, even though the wake structures generated by the hair resulted in a departure from the expected drag and lift behaviors, comparisons done with other experimenters’ results show that the outcomes from this study were strongly promising.

For future studies, several recommendations are provided. In the near-term, a re-evaluation of the current work without the hindrance of modeled hair should be done. Work done using a time-dependent computational approach should also be completed to further gauge the effects and inaccuracies of using the pseudo-transient method in relation to drag and lift. A keynote proposition would be the use of a wind tunnel experiment to acquire validation data. Ideally, this experiment would use live subjects of varying breast sizes in order to provide additional data in which to compare to the data herein. Additional research to evaluate the degree of which the information provided from this current work applies to real world situations should also be completed.

Acknowledgments

The author would like to send a massive thanks to the user “icemega5” found on both [Twitter](#) and [BowlRoll.net](#) for the Quetzalcoatl model. Without their work, this study would not have been possible. The author is grateful for his fellow colleagues for dedicating their time in helping proofread and provide guidance on this paper. Additionally, the author would like to make a shout out to users that frequent the [r/anime_irl](#) and [r/animemes](#) communities for their inspirational and fervent dissoluteness. Lastly, the author expresses gratitude towards both [Cool-Kyou Shinsha](#) and [Kyoto Animation](#) for their work on [Miss Kobayashi’s Dragon Maid](#).

The author received no funding for this research. The results of the present study do not constitute endorsement of any potential entity whether expressed or implied. Quetzalcoatl is also not the author’s “waifu”, although he respects her character as THE GODDESS OF THICC.

Appendix A: Supplementary Material

Additional contour plots in higher resolution and quality from the other velocities not examined in Section 4.2 can be found by following this link: <https://imgur.com/a/bz31B>.

A video further visualizing the flow structures in 3-D can be seen here: <https://youtu.be/1414xHh6tw0>.

The entire CFD study (project files and generated data) can be found by following:

https://mega.nz/#!lz5hzA5Q!JpG_t0IbflLuI24sC1pkV-C7nKW10xqZSMzBeH1Mt_A.

Appendix B: Additional Figures

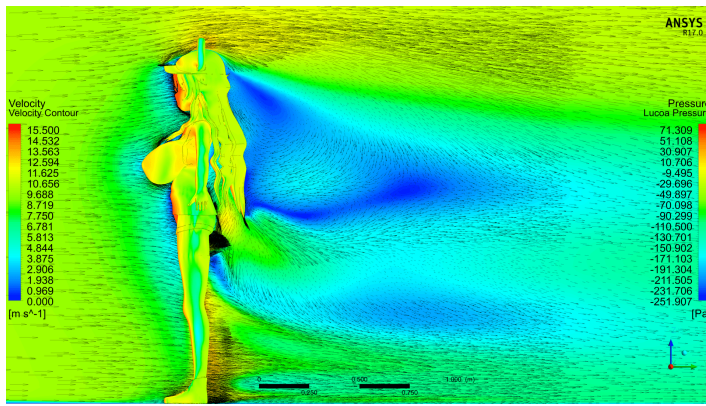


Figure 19. Velocity contours and vectors of the Normal model along the median plane.

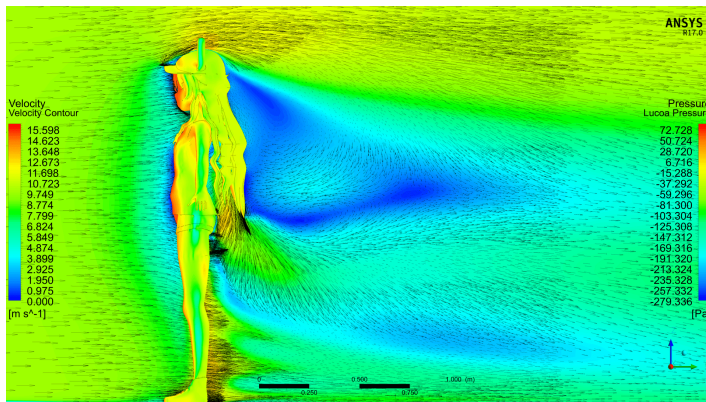


Figure 20. Velocity contours and vectors of the Flat model along the median plane.

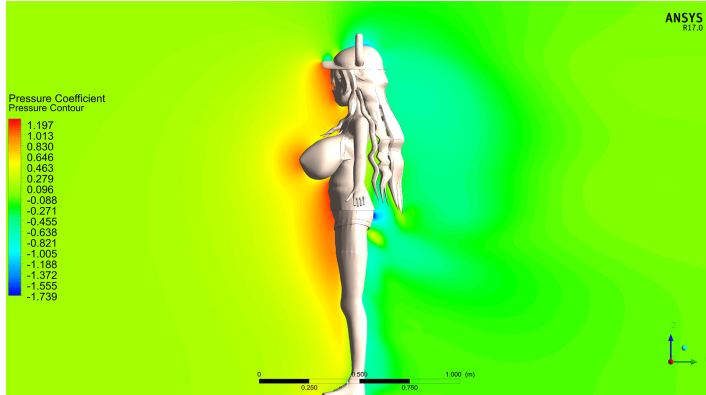


Figure 21. Pressure coefficient of the flow regime around the Normal model along the median plane.

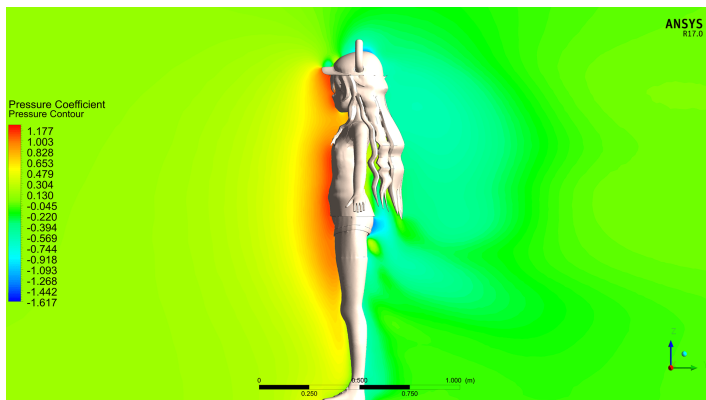


Figure 22. Pressure coefficient of the flow regime around the Flat model along the median plane.

References

- [1] A. V. Hill, "The air-resistance to a runner," *Proceedings of the Royal Society of London Series B Biological Sciences*, vol. 102, pp. 380-385, 1927.
- [2] C. T. Davies, "Effects of wind assistance and resistance on the forward motion of a runner," *Journal of Applied Physiology*, vol. 48, pp. 702-709, 1980.
- [3] J. A. Rodríguez-Marroyo, C.-E. Juneau, J. Peleteiro, A. C. Martínez and J. G. Villa, "Reference values and improvement of aerodynamic drag in professional cyclists," *Journal of Sports Sciences*, vol. 26, no. 3, 2008.
- [4] C. Barelle, "Sport Aerodynamics: On the Relevance of Aerodynamic Force Modelling Versus Wind Tunnel Testing," in *Wind Tunnels and Experimental Fluid Dynamics Research*, Rijeka, Croatia, InTech, pp. 349-368.
- [5] A. D'Auteuil, G. L. Larose and S. J. Zan, "Wind turbulence in speed skating: Measurement, simulation and its effect on aerodynamic drag," *Journal of Wind Engineering and Industrial Aerodynamics*, Vols. 104-106, pp. 585-593, 2012.
- [6] P. N. Doval, "Aerodynamic Analysis and Drag Coefficient Evaluation of Time-Trial Bicycle Riders," *Theses and Dissertations*, 2012.
- [7] T. J. Schmitt, "Wind-Tunnel Investigation of Air Loads on Human Beings," Defense Documentation Center for Scientific and Technical Information, Alexandria, Virginia, 1952.
- [8] G. J. v. Ingen-Schenau, "The influence of air friction in speed skating," *Journal of Biomechanics*, vol. 15, no. 6, pp. 449-458, 1982.
- [9] Triple Zed, "Flat Is Justice / Delicious Flat Chest | Know Your Meme," Literally Media Ltd., 30 August 2016. [Online]. Available: <http://knowyourmeme.com/memes/flat-is-justice-delicious-flat-chest>.
- [10] R. G. J. Flay, "Bluff Body Aerodynamics," in *Advanced Structural Wind Engineering*, Springer Japan, 2013, pp. 59-84.
- [11] L. W. Brownlie, "Aerodynamic characteristics of sports apparel," Canada, 1992.
- [12] D. Sumner, J. Heseltine and O. Dansereau, "Wake structure of a finite circular cylinder of small aspect ratio," *Exp Fluids*, vol. 37, pp. 720-730, 2004.
- [13] J. Okamoto and Y. Sunabashiri, "Vortex shedding from a circular cylinder of finite length placed on a ground plane," *ASME Journal of Fluids Engineering*, vol. 114, pp. 512-521, 1992.
- [14] Y. Zhou and M. M. Alam, "Wake of two interacting circular cylinders: A review," *International Journal of Heat and Fluid Flow*, vol. 62, pp. 510-537, 2016.
- [15] J. I. Choi and J. R. Edwards, "Large eddy simulation and zonal modeling of human-induced contaminant transport," *Indoor Air*, vol. 18, pp. 233-249, 2008.
- [16] Y. Tao, K. Inthavong and J. Tu, "Computational fluid dynamics study of human-induced wake and particle dispersion in indoor environment," *Indoor and Built Environment*, vol. 26, no. 2, pp. 185-198, 2016.
- [17] H. E. Lewis, A. R. Foster, B. J. Mullan, R. N. Cox and R. P. Clark, "Aerodynamics of the human microenvironment," *Lancet*, pp. 1273-1277, 1969.
- [18] S. Murakami, J. Zeng and T. Hayashi, "CFD analysis of wind environment around a human body," *Journal of Wind Engineering and Industrial Aerodynamics*, vol. 83, pp. 393-408, 1999.
- [19] C. Suárez, A. Iranzo, J. A. Salva, E. Tapia, G. Barea and J. Guerra, "Parametric Investigation Using Computational Fluid Dynamics of the HVAC Air Distribution in a Railway Vehicle for Representative Weather and Operating Conditions," *Energies*, vol. 10, no. 1074, pp. 1-13, 2017.
- [20] K. Inthavong, Y. Tao, P. Petersen, K. Mohanaragam, W. Yang and J. Tu, "A smoke visualisation technique for wake flow from a moving human manikin," *Journal of Visualization*, vol. 20, no. 1, pp. 125-137, 2017.
- [21] Y. Yan, X. Li, L. Yang and J. Tu, "Evaluation of manikin simplification methods for CFD simulations in occupied indoor environments," *Energy and Buildings*, vol. 127, 2016.
- [22] Google, "miss kobayashis dragon maid, 小林さんちのメイドラゴン - Google Trends," [Online]. Available: <https://trends.google.com/trends/explore?date=all&q=miss%20kobayashis%20dragon%20maid,%E5%B0%8F%E6%9E%97%E3%81%95%E3%82%93%E3%81%A1%E3%81%AE%E3%83%A1%E3%82%A4%E3%83%89%E3%83%A9%E3%82%B4%E3%83%B3>.
- [23] Samekichi Kiseki, "Miss Kobayashi's Dragon Maid | KnowYourMeme," Literally Media Ltd., 08 April 2017. [Online]. Available: <http://knowyourmeme.com/memes/subcultures/miss-kobayashis-dragon-maid>.
- [24] "Kobayashi-san Chi no Maid Dragon," [Online]. Available: <https://myanimelist.net/anime/33206>.
- [25] "Gag Boobs - TV Tropes," [Online]. Available: <http://tvtropes.org/pmwiki/pmwiki.php/Main/GagBoobs>.
- [26] RandomMan, "Anime Tiddies | Know Your Meme," Literally Media Ltd., 29 April 2015. [Online]. Available: <http://knowyourmeme.com/memes/anime-tiddies>.
- [27] "Quetzalcoatl | Kobayashi-san Chi no Maid Dragon Wiki | FANDOM powered by Wikia," 29 July 2017. [Online]. Available: <http://maid-dragon.wikia.com/wiki/Quetzalcoatl>.

- [28] "Official Statistics by Ministry of Education, Culture, Sports, Science and Technology," 28 March 2013. [Online]. Available: http://www.mext.go.jp/component/b_menu/other/_icsFiles/afldfile/2014/03/28/1345147_1.pdf.
- [29] icemega5, "ケツァルコアトル Ver. 1.00 - BowlRoll," BowlRoll, 11 July 2017. [Online]. Available: <https://bowlroll.net/file/141884>.
- [30] D. Tracey, "Standing, Line of Gravity at Joints, Postural Sway and Perturbations".
- [31] J. F. R. Mellveen, "The everyday effects of wind drag on people," *Weather*, vol. 57, pp. 410-413, November 2002.
- [32] D. E. McGhee and J. R. Steele, "Breast volume and bra size," *International Journal of Clothing Science and Technology*, vol. 23, no. 5, pp. 351-360, 2011.
- [33] Japanese Industrial Standards, *Sizing systems for foundation garments*, 1998.
- [34] H. Schlichting and K. Gersten, "Fundamentals of Boundary-Layer Theory," in *Boundary-Layer Theory*, Springer-Verlag Berlin Heidelberg, 2017, pp. 29-49.
- [35] F. Stern, "Flow Over Immersed Bodies," in *Mechanics of Fluids and Transport Processes*, 2014.
- [36] W. Donko, "Crunchyroll - FEATURE: Anime vs. Real Life - "Miss Kobayashi's Dragon Maid", Crunchyroll, 21 January 2017. [Online]. Available: www.crunchyroll.com/anime-feature/2017/01/21-1/feature-anime-vs-real-life-miss-kobayashis-dragon-maid.
- [37] Japan Meteorological Agency, "気象庁 | 過去の気象データ検索," [Online]. Available: http://www.data.jma.go.jp/obd/stats/etrn/view/nml_sfc_ym.php?prec_no=44&prec_ch=%93%8C%8B%9E%93s&block_no=47662&block_ch=%93%8C%8B%9E&year=&month=&day=&elm=normal&view=.
- [38] A. D'Auteuil, G. L. Larose and S. J. Zan, "Relevance of similitude parameters for drag reduction in sport aerodynamics," *Procedia Engineering* 2, pp. 2393-2398, 2010.
- [39] K. Aspelin, "Establishing Pedestrian Walking Speeds," Portland State University, Portland, Oregon, 2005.
- [40] Met Office, "Beaufort wind force scale," [Online]. Available: <https://www.metoffice.gov.uk/guide/weather/marine/beaufort-scale>.
- [41] C.-K. Choi and D.-K. Kwon, "Wind tunnel blockage effects on aerodynamic behavior of bluff body," *Wind and Structures*, vol. 1, no. 4, pp. 351-364, 1998.
- [42] M. Lanfrit, "Best practice guidelines for handling Automotive External Aerodynamics with FLUENT," Darmstadt, Germany, 2005.
- [43] G. Balafas, "Polyhedral Mesh Generation for CFD-Analysis of Complex Structures," 2014.
- [44] M. Spiegel, T. Redel, Y. J. Zhang, T. Struffert, J. Hornegger, R. G. Grossman, A. Doerfler and C. Karmonik, "Tetrahedral vs. polyhedral mesh size evaluation on flow velocity and wall shear stress for cerebral hemodynamic simulation," *Computer Methods in Biomechanics and Biomedical Engineering*, pp. 1-10, 2010.
- [45] B. Sasanapuri, R. Steed and V. Veera, "ANSYS CFD Results for the AIAA 2nd High Lift Prediction Workshop," in *AIAA 2nd High Lift Prediction Workshop*, San Diego, 2013.
- [46] ANSYS® FLUENT, *Release 17.0, Help System, Theory Guide*, ANSYS, Inc..
- [47] F. R. Menter, "Zonal Two Equation $k-\omega$ Turbulence Models for Aerodynamic Flows," in *24th Fluid Dynamics Conference*, Orlando, Florida, 1993.
- [48] S. V. Patankar, *Numerical Heat Transfer and Fluid Flow*, Washington, DC: Hemisphere, 1980.
- [49] D. J. Mavriplis, "Revisiting the Least-squares Procedure for Gradient Reconstruction on Unstructured Meshes," National Institute of Aerospace, Hampton, Virginia, 2003.
- [50] Z. J. Chen and A. J. Przekwas, "A coupled pressure-based computational method for incompressible/compressible flows," *Journal of Computational Physics*, vol. 229, no. 24, pp. 9150-9165, 2010.
- [51] S. P. Mathiyalagan and B. H. L. Gowda, "Reverse Flow in Converging Channels with Obstruction at the Entry," in *Fluid Mechanics and Fluid Power – Contemporary Research: Proceedings of the 5th International and 41st National Conference of FMFP 2014*, Kanpur, India, Springer, 2017, pp. 287-298.
- [52] R. S. Khan and S. Umale, "CFD Aerodynamic Analysis of Ahmed Body," *International Journal of Engineering Trends and Technology*, vol. 18, no. 7, pp. 301-308, 2014.
- [53] D. P. Tselepidakis and L. Collins, "Verification and Validation in CFD and Heat Transfer: ANSYS Practice and the New ASME Standard," in *ASME 2012 Verification and Validation Symposium*, 2012.
- [54] M. Kuntz, "Validation and Verification of ANSYS Internal Combustion Engine Software," in *2012 Automotive Simulation World Congress*, Detroit, 2012.
- [55] B. A. Edge, E. G. Paterson and G. S. Settles, "Computational Study of the Wake and Contaminant Transport of a Walking Human," *Journal of Fluids Engineering*, vol. 127, no. 5, pp. 967-977, 2005.
- [56] T. S. Coffey, C. T. Kelley and D. E. Keyes, "Pseudo-Transient Continuation and Differential-Algebraic Equations," Center for Research in Scientific Computation, Raleigh, NC, 2002.
- [57] M. Keating, "Accelerating CFD Solutions," *ANSYS Advantage*, pp. 48-49, 2011.
- [58] C. T. Kelley and D. E. Keyes, "Convergence Analysis of Pseudo-Transient Continuation," *Society for Industrial and Applied Mathematics*, vol. 35, no. 2, pp. 508-523, 1998.
- [59] ANSYS, *Introduction to ANSYS FLUENT: Lecture 4 - Solver Settings*, ANSYS, 2012.
- [60] U.S. Department of Defense, "Verification, Validation, and Accreditation (VV&A) Recommended Practices Guide," Defense Modeling and Simulation Office, Office of the Director of Defense Research and Engineering, Virginia, 1996.
- [61] NASA NPARC Alliance Verification and Validation, "Examining Spatial (Grid) Convergence," [Online]. Available: <http://www.grc.nasa.gov/WWW/wind/valid/tutorial/spatconv.html>.
- [62] ASME, "Guide for Verification and Validation in Computational Solid Mechanics," American Society of Mechanical Engineers, Virginia, 2006.
- [63] P. J. Roache, "Verification and validation in computational science and engineering," *Computing in Science Engineering*, no. 1, pp. 8-9, 1998.
- [64] ASME, "Procedure for Estimation and Reporting of Uncertainty Due to Discretization in CFD Applications," American Society of Mechanical Engineers, Virginia, 2008.
- [65] L. Kwaśniewski, "Application of grid convergence index in FE computation," *Bulletin of The Polish Academy of Sciences: Technical Sciences*, vol. 61, no. 1, pp. 123-128, 2013.
- [66] J. R. Shanebrook and R. D. Jaszczak, "Aerodynamic drag analysis of runners," *Medicine and Science in Sports and Exercise*, vol. 8, pp. 43-45, 1976.
- [67] A. D. Penwarden, P. F. Grigg and R. Rayment, "Measurements of Wind Drag on People Standing in a Wind Tunnel," *Building and Environment*, vol. 13, pp. 75-84, 1977.
- [68] L. Brownlie, I. Mekjavic, I. Gartshore, B. Mutch and E. Banister, "The influence of apparel on aerodynamic drag," *The Annals of Physiological Anthropology*, vol. 6, no. 3, pp. 133-143, 1987.
- [69] J. J. H. Gómez, V. Marquina and R. W. Gómez, "On the performance of Usain Bolt in the 100m sprint," *European Journal of Physics*, vol. 34, pp. 1227-1233, 2013.
- [70] T. Inoue, T. Okayama, T. Teraoka, S. Maeno and K. Hirata, "Wind-tunnel experiment on aerodynamic characteristics of a runner using a moving-belt system," *Cogent Engineering*, 2016.
- [71] J.-L. Aider, J.-F. Beaudoin and J. E. Wesfreid, "Drag and lift reduction of a 3D bluff-body using active vortex generators," *Experimental Fluids*, vol. 48, pp. 771-789, 2010.
- [72] "The Win Tunnel: When is a hairdo a hairdon't?," *Specialized Bicycles*, [Online]. Available: https://youtu.be/Lf5jL__kws0.